Leading baryon production in $p+A$ collisions at relativistic energies

K. N. Barish,[1] S. Batsouli,[2] S. J. Bennett,[3] M. Bertaina,[4,*] A. Chikanian,[2] T. M. Cormier,[3] P. Fachini,[3] B. Fadem,[5] L. E. Finch,[2] N. K. George,[2] S. V. Greene,[6] P. Haridas,[4] J. C. Hill,[5] A. S. Hirsch,[7] R. Hoversten,[5] H. Z. Huang,[8] H. Jaradat,[3] T. Lainis,[9] J. G. Lajoie,[5] Q. Li,[3] H. Long,[8] C. Maguire,[6] R. D. Majka,[2] T. E. Miller,[6] M. G. Munhoz,[3] J. L. Nagle,[10] A. Petridis,[5] I. A. Pless,[4] N. T. Porile,[7] C. A. Pruneau,[3] M. S. Z. Rabin,[11] J. D. Reid,[6] A. Rose,[6] J. Sandweiss,[2] R. P. Scharenberg,[7] A. J. Slaughter,[2] A. Tai,[8] G. Van Buren,[8,†] F. K. Wohn,[5] Z. Xu,[2] and E. Yamamoto[8]

(The E941 Collaboration)

[1]*University of California at Riverside, Riverside, California 92521*
[2]*Yale University, New Haven, Connecticut 06520*
[3]*Wayne State University, Detroit, Michigan 48201*
[4]*Massachusetts Institute of Technology, Cambridge, Massachusetts 02139*
[5]*Iowa State University, Ames, Iowa 50011*
[6]*Vanderbilt University, Nashville, Tennessee 37235*
[7]*Purdue University, West Lafayette, Indiana 47907*
[8]*University of California at Los Angeles, Los Angeles, California 90095*
[9]*United States Military Academy, West Point, New York 10996*
[10]*Columbia University, Nevis Laboratory, Irvington, New York 10533*
[11]*University of Massachusetts, Amherst, Massachusetts 01003*

(Received 6 July 2001; published 3 December 2001)

Invariant multiplicity distributions of the leading neutron and proton have been measured in minimum bias $p+$Be, $p+$Al, $p+$Cu, and $p+$Pb collisions at 19 GeV/c and $p+$Be and $p+$Pb collisions at 12 GeV/c with the E864/E941 spectrometer at the Alternating Gradient Synchrotron (AGS). The experimental acceptance for the measurement covers a rapidity region of $1.7 \leqslant y \leqslant 3.3$ and transverse momentum region of 0.075 GeV/c $\leqslant p_T \leqslant$ 1.025 GeV/c. The leading proton and leading neutron production, as a function of the light cone momentum fraction x_+, show energy scaling at AGS energies. The proton/neutron ratio, $(dN/dx_+)_p/(dN/dx_+)_n$, decreases from about 5.0 near beam rapidity to about one at midrapidity. The ratio has no strong target dependence as a function of rapidity. The target dependence of the leading proton distribution as a function of x_+ demonstrates an approximate energy scaling from the AGS to the Super Proton Synchrotron.

DOI: 10.1103/PhysRevC.65.014904 PACS number(s): 25.40.Kv, 13.85.Ni

I. INTRODUCTION

Baryon number transport in $p+A$ collisions has been an important topic since it is closely related to mechanisms leading to high energy and/or baryon number densities in ultrarelativistic heavy ion collisions. Busza and Goldhaber pioneered the study of proton rapidity loss based on a semi-inclusive measurement of the proton in the Feynman variable x_F and transverse momentum p_T from $p+A$ collisions [1]. They deduced a mean rapidity loss of over two units in central $p+A$ collisions, from which it was predicted that nuclear matter of very high baryon density would be formed in nucleus-nucleus collisions at the Alternating Gradient Synchrotron (AGS). Experimental measurements of the proton rapidity density distributions at the AGS bore out this prediction [2]. The energy loss of the incident proton was presumed to contribute to particle production at midrapidity and thus was directly related to the energy density that may be achieved in nuclear collisions. Experimentally, however, it was found that even in central $p+A$ collisions where the incident proton loses a significant fraction of its momentum, there are a few very fast particles that carry away a significant fraction of the total momentum [3]. Thus, the amount of energy deposited at midrapidity for particle production is significantly smaller than what is indicated by the proton rapidity loss alone. The physical picture that has emerged is that the incident proton fragments, producing leading particles in $p+A$ collisions. The proton rapidity loss in $p+A$ collisions only indicates the baryon number transport in the fragmentation process. A comprehensive study of all leading particles will provide important insight to the fragmentation process and relate to both the energy deposition and net baryon density in high energy nucleus-nucleus collisions.

A leading particle here refers to the produced particle that carries the highest momentum in a $p+A$ collision. Experimentally, however, this cannot always be unambiguously defined in an inclusive measurement with incomplete acceptance like experiment E941, where not all the produced particles in an event are detected. In this paper, using the convention in Ref. [4], we assume a measured baryon is a leading baryon if it has a rapidity larger than $y_{cm}=0.5y_b$, where y_b is the beam rapidity. This assumption is approximately true since the baryon pair production cross section is relatively small at AGS energies.

*Present address: Dipartimento di Fisica Generale, Universita' di Torino, Italy.

†Present address: Brookhaven National Laboratory, Upton, New York 11973.

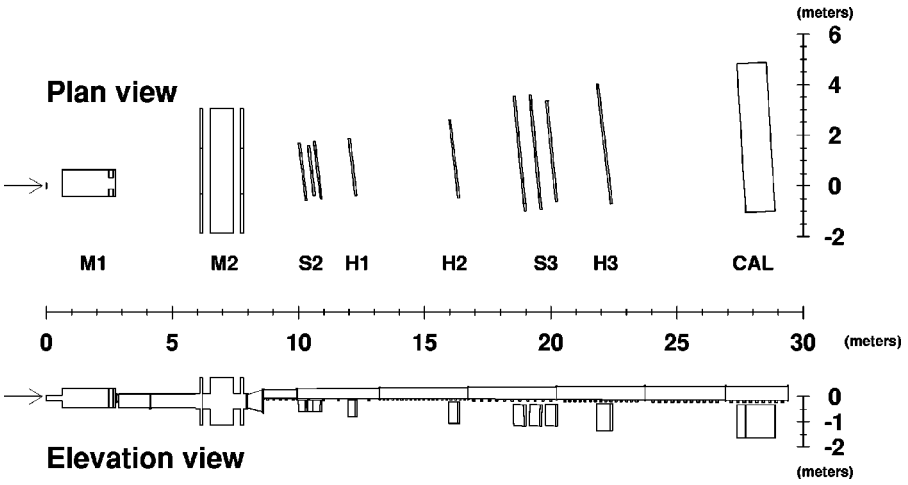

FIG. 1. The E864/E941 spectrometer in plan and elevation views, showing the dipole magnets (M1 and M2), hodoscopes (H1, H2, and H3), straw tube arrays (S2 and S3), and hadronic calorimeter(CAL). The narrow rectangles surrounding M2 are the shield plates and the target position is pointed by the arrow in front of M1. The vacuum chamber is not shown in the plan view.

The emerging baryon, which carries the original baryon number of the incident proton, may be a proton, a neutron, or a hyperon. Previous $p+A$ experiments [5–10] have systematically studied leading proton production at both AGS and SPS energies with various targets. There have been, however, no systematic studies of leading neutrons in $p+A$ collisions. The previous measurement of leading neutron production in $p+A$ collisions [7] suffered from very limited statistics.

Leading neutrons represent a significant fraction of the emerging baryons in $p+A$ collisions. In $p+\mathrm{Pb}$ collisions at 19 GeV/c, the relativistic quantum molecular dynamics (RQMD) model [11], for example, predicts that about 34% of the emerging particles with the highest momentum are protons and 25% are neutrons. This reflects a significant cross section for the isospin exchange reaction $p+A\rightarrow n+X$. Essentially all theoretical models (Refs. [12–14], for instance) are only constrained by the measurement of leading protons. Typically these models use parametrized functions to describe the process of an incident proton fragmenting into a leading proton in $p+A$ collisions. With a set of well-tuned parameters, these theoretical models can usually reproduce the existing experimental $p+A$ data for leading proton yields, although underlying physical pictures are very different. The extrapolation of these models from $p+A$ to $A+A$ collisions, however, yields drastically different predictions for baryon rapidity distributions in high energy $A+A$ collisions [15]. This discrepancy in predictions may be indicative that current parametrizations for the proton fragmentation process do not accurately describe the underlying dynamics, presumably due to the lack of detailed experimental constraints on leading neutron yields. Systematic measurements of leading baryons including both protons and neutrons will better constrain theoretical descriptions for $p+A$ collisions and help to develop a comprehensive understanding of the dynamics.

The E941 experiment at Brookhaven National Laboratory was designed to measure leading protons and neutrons in $p+A$ collisions. Following this introduction, we will in Sec. II briefly describe the E941 experimental setup, and then give a detailed description of the data analysis techniques that were used to obtain the invariant multiplicities for protons and neutrons. In Sec. III we will present E941 measurements of leading neutrons and protons in $p+A$ collisions at two beam momenta using the E864/E941 spectrometer. The energy and target dependence of leading proton and neutron production will be presented. We will also compare our data with RQMD calculations and our proton data with other experiments at various energies.

II. EXPERIMENTAL DESCRIPTION

A. The E941 spectrometer

Figure 1 shows both plan and elevation views of the E941 spectrometer, which is essentially the same as the E864 spectrometer [16]. Here, we only briefly describe the spectrometer. A more detailed description of the apparatus can be found in Ref. [16].

Beam counters and a multiplicity counter near the target formed the first level trigger for the experiment (they are not shown in Fig. 1). The multiplicity counter was a scintillating annulus placed around the beam pipe and subtended the angular range of 5.0°–45.0°. The multiplicity counter trigger threshold level was set below the minimum ionizing particle peak produced by the detector. Our simulation shows that for inelastic $p+A$ interactions the multiplicity counter recorded about 95% of the total inelastic interaction and the fraction varied slightly with target and beam momentum. The interaction products then traveled downstream through two diple magnets M1 and M2. Two magnetic field settings of $+0.2$ T and -0.2 T were used in the experiment. A collimator inside M1 defined the experimental acceptance, which was approximately -32 to 114 mrad horizontally and -17 to -51.3 mrad vertically for neutral particles.

The E941 tracking system consisted of three segmented scintillating hodoscopes (H1, H2, and H3), two straw tube wire tracking chambers (S2 and S3) [17], and a spaghetti hadronic calorimeter (CAL) [18] located behind the tracking system. Incident protons that did not interact in the target continued downstream through a vacuum chamber. This vacuum chamber extended through the M1 and M2 magnets to the end of the spectrometer. A small rectangular array of four scintillation counters was placed behind the exit of the vacuum chamber to measure incident protons that did not interact in the target. The E941 spectrometer was located

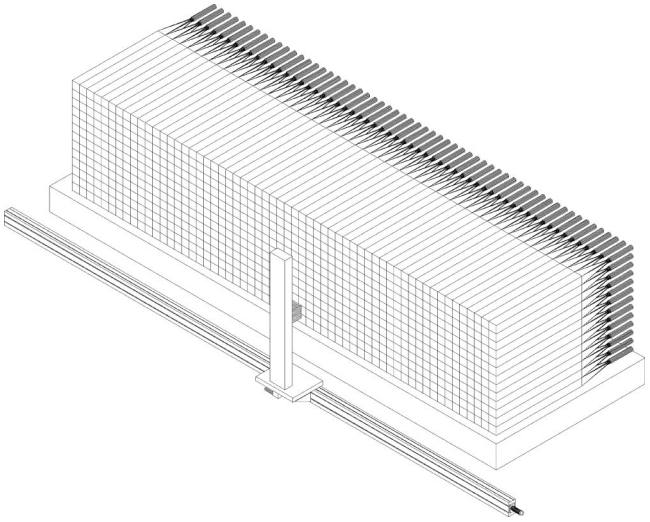

FIG. 2. The E864/E941 hadronic calorimeter; an array of 58 $\times$13 towers. The active material is scintillating fiber running lengthwise down each lead tower in a spaghetti design. Also pictured is the cobalt-60 calibration system, which is used for gain matching among the towers.

underneath the vacuum chamber. The experimental acceptance for leading baryon measurements covered a region of $1.7 \leqslant y \leqslant 3.3$ and $0.075\ \text{GeV}/c \leqslant p_T \leqslant 1.025\ \text{GeV}/c$.

The hodoscopes were used for finding charged track candidates via linear fits to the space-time points of hits in the three hodoscope planes. These candidate tracks were projected to the straw chambers to locate associated straw tube hits, which were used to improve the tracking position resolution. For tracks that came from the target, the rigidities were obtained from the curvature of the track as it traversed the dipole magnets. The tracking procedure also yielded a velocity for the track based on the time-of-flight measurement of the hodoscope counters. The charge of the track was calculated from the dE/dx energy deposition in the hodoscope counters. We calculated the mass of the charged particles from the momentum and the velocity measurements. The time resolution of the hodoscopes was about 140 ps and the typical mass resolution was about 6% for the data presented here.

The spaghetti hadronic calorimeter, shown in Fig. 2 schematically, was the essential detector for measurement of neutral particles. The calorimeter was made of lead and scintillator fibers in a spaghetti design. E864 was the first major experiment that used this new type of detector technology to measure both the energy and timing information. The detector consisted of an array of 58×13 towers, each 10 $\times10$ cm on the front face [18]. The spaghetti calorimeter provided an excellent timing resolution of $\sigma_t = 400$ ps and an energy resolution of $3.5\% + 34.4\%/\sqrt{E}$ for hadrons, where E is the energy in GeV deposited in the calorimeter. The calorimeter measurement of the energy deposition and the time-of-flight of hadrons, coupled with the veto of charged particles from the tracking system, was used to identify neutral particles. The veto efficiencies for proton tracks are about 95%; see Sec. II D for details.

In the $p+A$ experiment, three modifications were made from the E864 spectrometer: (1) the quartz Cerenkov beam counters [19] were replaced with new scintillating counters for $p+A$ running; (2) a new multiplicity counter was installed to cover more solid angle for triggering on inelastic $p+A$ collisions; and (3) the small rectangular array of four quartz detectors at the end of the spectrometer was replaced by four scintillation counters. Position scans of the proton beam profile after traversing the dipole magnets and detailed knowledge of the magnetic field in the E941 spectrometer yielded a precise measurement of the incident proton beam momentum.

The E941 experiment used two nominal beam momentum settings, 12 GeV/c and 19 GeV/c, and four targets, Be, Al, Cu and Pb. The actual momenta of the incident protons were measured during the experiment to be 12.05 GeV/c and 18.94 GeV/c, respectively. The data analyzed in this work were taken using targets of 1.52 cm thickness. Data were also taken with no target (empty target) to correct for background from non-target interactions.

In addition to the interaction trigger based on the multiplicity counter, a spectrometer trigger was set up for the experiment using the so-called late-energy trigger (LET), essentially demanding that a minimum of 0.3 GeV energy was deposited in any of the inner towers of the calorimeter, explicitly excluding the edge towers. Details of the LET setup can be found in Ref. [20]. The spectrometer trigger was employed as a level-1 trigger. The interaction trigger (level 0), gated by the beam counters, initiated a data acquisition sequence. If the event failed to generate a spectrometer trigger, the data acquisition sequence was aborted. The spectrometer trigger enhanced the number of particles in the spectrometer in our data sample by approximately a factor of 10 (at 19 GeV/c) and 17 (at 12 GeV/c).

The 19 GeV/c data used in this paper contained about 20×10^6 events for each target with the spectrometer trigger, about half of which were from a -0.2 T run and the other half from a $+0.2$ T run. The 12 GeV/c data contained about 10×10^6 -0.2 T triggered events for each target. Two magnetic field settings were used in order to increase p_T coverage of the proton measurement and to estimate systematic errors in our analysis.

B. Neutron reconstruction

We start cluster reconstruction of hadronic showers in the calorimeter by searching for peak towers in an event. We define a peak tower as a tower that has at least 0.5 GeV energy deposition and in which the energy is greater than any of its eight neighbors in a 3×3 array. An energy shower is then reconstructed by including all towers in a 3×3 array centered on a peak tower.

We have applied the method developed by the E864 analysis [21] to isolate neutron showers in cluster reconstruction. A set of cuts was used to remove contamination from photons and other sources. We briefly review those cuts here:

(1) The peak tower of the shower must be at least two towers inside the calorimeter volume, which defines a fiducial region for the calorimeter acceptance.

(2) There must be no charged particle track found by the tracking system that points to any of the 3×3 tower array, centered on the peak tower.

(3) There must be no other peak tower having an energy larger than $E_{\rm pk}$ in the 16 towers surrounding the 3×3 array of the reconstructed shower. The $E_{\rm pk}$ used in the analysis ranged from 1.5 to 2.5 GeV depending on the rapidity of the shower.

(4) The ratio of total energy in a 5×5 array to that in the 3×3 array inside, $R_{5\times5/3\times3}$, must be smaller than a maximum allowable value that ranged from 1.7 to 2.5.

(5) All towers of the shower that register a timing measurement must have a timing within a windowr $t_{\rm max}$ of the peak tower. The $t_{\rm max}$ was between 1.6 ns and 1.75 ns.

(6) For rapidity $\geqslant2.5$, a cut ($\leqslant0.83$) on the ratio of the peak tower energy to the total energy in the 3×3 array was used to reduce contamination from photons.

(7) The shower energy profile was compared with the energy profiles of several hundred thousand isolated proton showers. The fraction of shower energy in each tower of the 3×3 array was rounded to the nearest 5%. The nine fractions were compared with the corresponding nine fractions for each of these isolated proton showers. Two showers were identified as having the same shower shape if all the nine fractions of the two showers were matched. A neutral shower was discarded if less than two identical proton shower shapes were found.

The velocity of the shower particle is obtained from the peak tower time and the shower position assuming a straight line trajectory from the target. The mass of the reconstructed shower is then calculated from the energy sum of the 3×3 tower array and the Lorentz factor $\gamma_{\rm peak}$ from the velocity, $m=E_{3\times3}/(\gamma_{\rm peak}-1)$.

Figure 3 shows the neutron acceptance in the p_T-y phase space in the calorimeter. The largest acceptance efficiency has a value about 20%, which contains both the geometric acceptance and the reconstruction efficiency. However, the charged track veto efficiencies are not included in this calculation and they will be discussed separately in Sec. II D. We divide the p_T-y phase space into bins of 50 MeV/c in p_T and 0.2 in rapidity. For each bin we make a mass plot as shown in Fig. 4. There is a low mass background for rapidity bins below 2.9 due to photons and scattered hadrons [21]. We determine the number of neutrons by counting particles with mass above 0.55 GeV/c^2 subtracted by appropriate background underneath the signal. The low mass background in each mass distribution is fitted by both a Gaussian and an exponential function and the signal is fitted by a Gaussian function, as shown in Fig. 4(a) as an example of the exponential background fit. The difference resulting from these two background subtraction schemes is included in the systematic error. The magnitude of the neutron background decreases as a function of rapidity, typically around 10% at $y=1.7$ and 3% at $y=2.7$.

For those showers with a velocity very close to one ($c=1$) we do not have sufficient resolution to accurately determine the mass of the particles. We assume these showers to be neutrons if their rapidities $\geqslant2.9$ (in this case, the rapidity of a shower is calculated using energy information only) and they survive the charged particle veto procedure. As indicated in Fig. 4(b), there is no noticeable low mass background at high rapidity. Once a neutral particle is determined to be a neutron, the known neutron mass is used to calculate other kinematic variables.

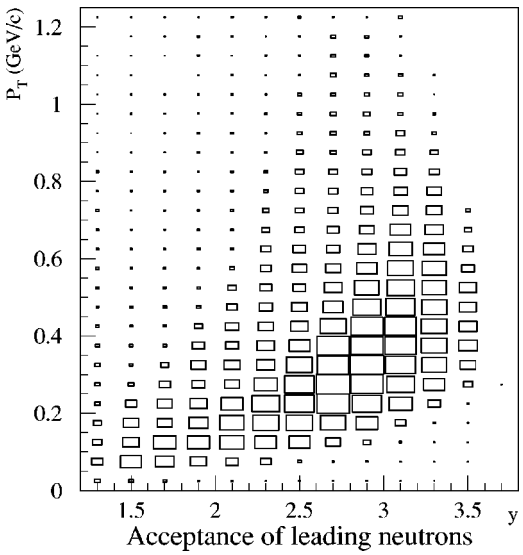

FIG. 3. Neutron acceptance in the p_T-y phase space in the calorimeter.

C. Proton reconstruction

Proton tracks are reconstructed primarily using the hodoscope (H1/H2/H3) and straw chamber (S2/S3) detectors. The tracking procedure has been described elsewhere [16]. We summarize here several relevant cuts that were used in our analysis.

(1) A track must be within the fiducial region defined using hodoscope, straw chamber, and calorimeter detectors.

(2) The charge measured by each hodoscope plane must be between 0.87e and 1.75e.

(3) The vertical intercept of a track at the target must be between -3.2 cm and 2.8 cm. This cut helps ensure that a track is from the target.

(4) Values of χ^2 per degree of freedom from linear fits of a track in various space-time projections must be smaller than a cut ranging from 2.5 to 3.9 depending on the space-time quantities used in the fits.

(5) In order to minimize background it is also required that a track be associated with a peak tower in the calorimeter.

For those tracks that survive the above cuts, mass can be calculated provided that the velocity of the track is smaller than one. Figure 5 shows the mass spectra of positively charged tracks in two p_T-y bins. Similar to the neutron measurement using the measured mass spectrum in each p_T-y bin, we count protons for mass >0.65 GeV/c^2 (an upper-bound mass <1.5 GeV/c^2 is also used for $y<2.3$ to avoid counting deuterons), subtracted by an appropriate background as shown in Fig. 5, in which both the background and signal are fitted by a Gaussian function. The proton background increases from low rapidity bins (2% at $y=1.7$) to

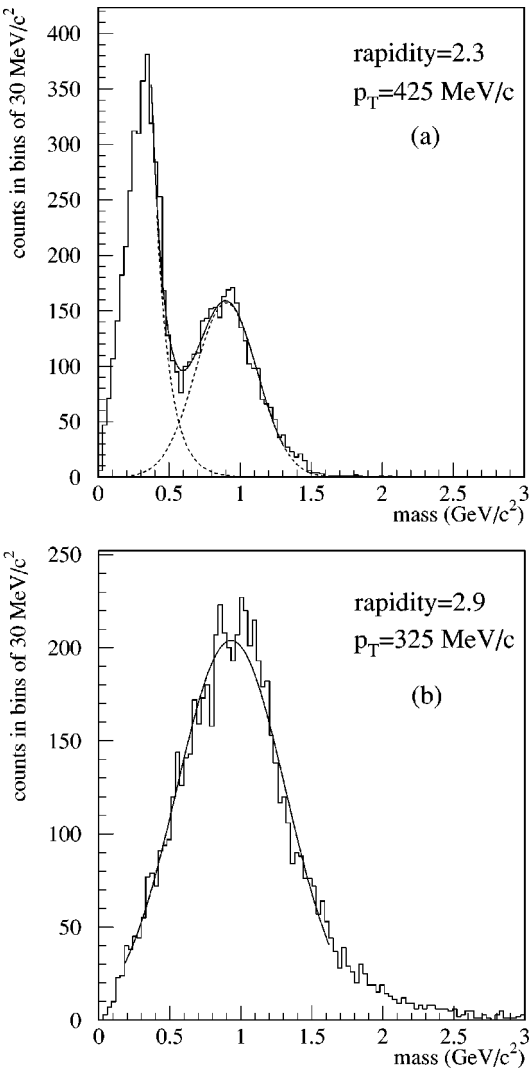

FIG. 4. Sample neutron mass histograms in two bins: (a) $y=2.2$–$2.4(400<p_T<450$ MeV/$c)$ and (b) $y=2.8$–$3.0(300<p_T<350$ MeV/$c)$.

high rapidity bins (10% at $y=2.7$) due to the decreasing mass resolution of our tracking system. However, the background drops rapidly near the beam rapidity ($y=3.1$ and 3.3) since there is little contamination from other particles (π^+ and K^+) in this region. Those tracks with a velocity very close to 1, for which we cannot determine the mass with sufficient resolution, we assume to be protons provided that their momenta are greater than a given cut (11.0 GeV/c for 19 GeV/c data and 9.0 GeV/c for the 12 GeV/c data). Contamination from other charged particles in the proton sample after this momentum cut is estimated to be smaller than 1% based on RQMD simulations. The proton acceptance, determined by the tracking system, covers a phase space region similar to the neutron acceptance shown in Fig. 3.

D. Data analysis for invariant multiplicity

The invariant multiplicity for each Δp_T-Δy bin was obtained by

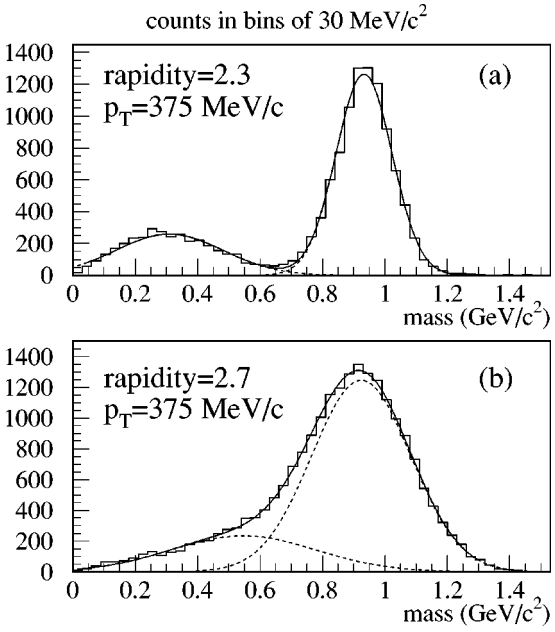

FIG. 5. Sample proton mass histograms in two bins: (a) $y=2.2$–2.4 and (b) $y=2.6$–2.8 $(350<p_T<400$ MeV/$c)$. Note that rapidities of all tracks are calculated assuming proton mass.

$$\frac{1}{2\pi p_T}\frac{d^2N}{dydp_T} = \frac{1}{2\pi p_T \Delta y \Delta p_T}\frac{1}{\epsilon_{\rm acc}(y,p_T)\epsilon_{\rm rec}(y,p_T)}\frac{1}{1-r_{\rm em}-r_\delta} \times\left[\frac{N_{\rm counts}(y,p_T)}{N_{\rm events}} - r_{\rm em}\frac{N^{\rm em}_{\rm counts}(y,p_T)}{N^{\rm em}_{\rm events}}\right], \quad (1)$$

where $N_{\rm counts}(y,p_T)$ and $N^{\rm em}_{\rm counts}(y,p_T)$ are the number of background-subtracted neutrons or protons reconstructed in $N_{\rm events}$ target events and $N^{\rm em}_{\rm events}$ empty target events, respectively; $\epsilon_{\rm acc}(y,p_T)$ are the geometric acceptances for neutrons or protons in the fiducial volume of the spectrometer; $\epsilon_{\rm rec}(y,p_T)$ are the reconstruction efficiencies of those accepted particles; and $r_{\rm em}$ and r_δ are the fraction of the empty target and δ ray interactions in the target runs.

The $\epsilon_{\rm acc}(y,p_T)$ were obtained by a GEANT simulation using RQMD as the input distribution. For calculating neutron reconstruction efficiencies, neutron showers were faked using a library of isolated proton showers from the E941 data. The proton showers were identified by the tracking system and contamination cuts in the calorimeter were applied to select clean showers. Each fake neutron shower was then superimposed on a real event in the calorimeter to determine the $\epsilon_{\rm rec}(y,p_T)$ for neutrons. The neutron reconstruction efficiencies were found to be typically about 50%. The $\epsilon_{\rm rec}(y,p_T)$ for protons were obtained in a similar way, but this time an RQMD proton track was embedded in all charged track detectors in an event. The proton reconstruction efficiencies were typically about 70%. For the proton measurement, we had also taken into account the hardware inefficiency of the tracking system, which was not included

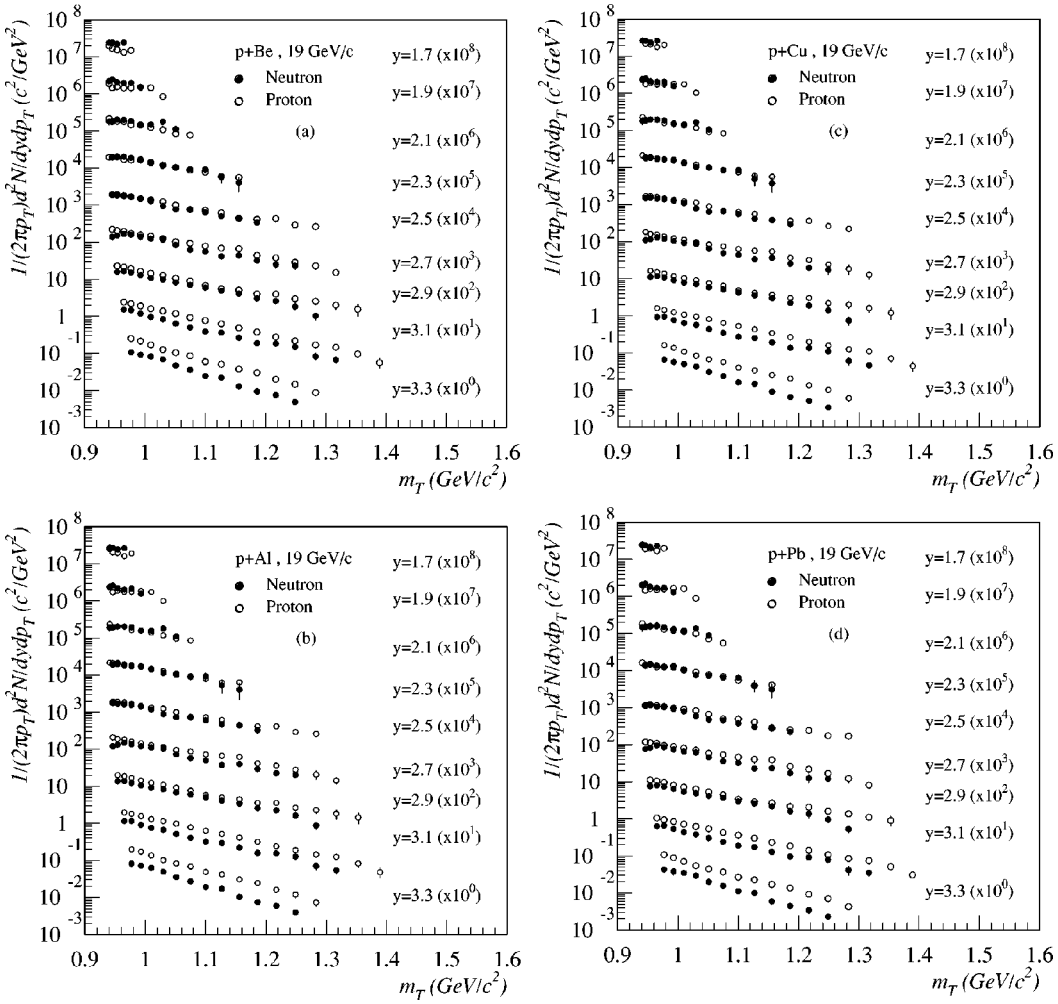

FIG. 6. Neutron and proton invariant multiplicities in (a) $p+\mathrm{Be}$, (b) $p+\mathrm{Al}$, (c) $p+\mathrm{Cu}$, and (d) $p+\mathrm{Pb}$ collisions at 19 GeV/c as a function of transverse mass for different rapidity bins. The multiplicity of each rapidity bin is multiplied by a successive factor of 10 for presentational purposes.

in the calculation of the reconstruction efficiencies. This detector efficiency was found to be about 95% using real data.

The multiplicity counter was sensitive to δ ray electrons knocked out of the target by incident protons. The incident protons, however, would suffer little perturbation in their trajectory if no inelastic collision took place. The four scintillation counters, which were designed to measure the beam protons at the end of the E941 spectrometer, were used to correct for δ ray induced multiplicity triggers. The empty target runs were analyzed in the same procedure as that for real target runs. We corrected for the empty target contribution in each phase space bin.

The r_{em} and r_{δ} were found to be about 5%–10% and 23%–55%, respectively, depending on the target and incident momentum. The r_{δ} was calculated using information from the four scintillation counters in the beam line at the end of the spectrometer. It was also estimated from the known interaction length of the target and the measured multiplicity trigger rate taking into account the multiplicity counter efficiency. Results obtained from the two methods were in good agreement with each other. We estimated that the systematic error from δ ray interactions was about 5%.

We have also made corrections for particles that were scattered into the fiducial volume of the spectrometer, mostly from the collimator. For the proton measurement, these scattered particles were removed by a cut on the track projection to the target location. For the neutron measurement, however, we had to use Monte Carlo simulations to estimate this background in each phase space bin. We used RQMD Monte Carlo events to estimate the background for neutrons after they scaled to reproduce the background for protons. The correction factor for neutrons ranged from 6% ($y=3.3$) to 17% ($y=1.7$).

Some proton showers were mistaken for neutrons because the proton tracks were not reconstructed in our veto procedure for charged particles. Most of these misidentified showers were due to protons that had scattered off the vacuum chamber into the spectrometer. In doing so, the protons missed at least one hodoscope plane. The correction was found to be around 5% through a simulation using RQMD events and was made for each p_T-y bin. In the low rapidity region there was also K_L contamination to neutron showers [21], which was believed to be small and treated as part of the low mass background.

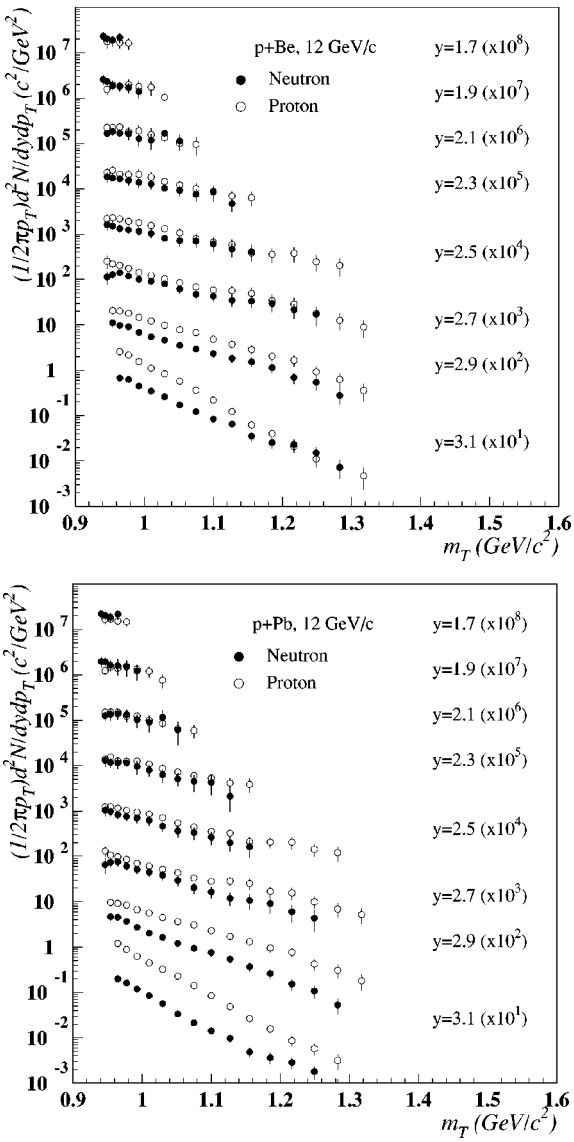

FIG. 7. Neutron and proton invariant multiplicities in (a) $p+$Be and (b) $p+$Pb collisions at 12 GeV/c as a function of transverse mass for different rapidity bins. The multiplicity of each rapidity bin is multiplied by a successive factor of 10 for presentational purposes.

Finally we have also subtracted those neutrons or protons due to hyperon (mostly Λ) feed-down from measured multiplicities. The bin by bin correction was found to be of the order of 5% based on RQMD simulations.

III. RESULTS AND DISCUSSION

Figures 6 and 7 show proton and neutron invariant multiplicity distributions as a function of m_T ($\equiv\sqrt{m_0^2+p_T^2}$) for all four targets at 19 GeV/c and two targets at 12 GeV/c. Measurements in each rapidity bin are multiplied by different orders of 10 for presentation purposes. The errors shown in the invariant multiplicity distributions contain both statistical and systematic errors. The shapes of the proton and neutron distributions at the same rapidity are very similar. The proton invariant multiplicities are higher than those of neutrons in the high rapidity region. However, the proton and neutron yields seem to quickly approach each other at midrapidity.

For the rapidity bins of $y\geqslant 2.3$, where we have sufficient coverage in transverse momentum, we fit the leading baryon spectra with Boltzmann distributions in transverse mass,

$$\frac{1}{2\pi p_T}\frac{d^2N}{dydp_T}\equiv\frac{1}{2\pi m_T}\frac{d^2N}{dydm_T}=Am_T\exp(-m_T/T). \tag{2}$$

The extracted inverse slope parameters T are shown in Tables I and II. The inverse slope parameters are about the same for proton and neutron and slightly decrease with increasing rapidity. The inverse slope parameters show little target dependence. The magnitude of the inverse slope parameters and their dependence on target and rapidity derived from our data are consistent with the E802 experiment proton measurement [9]. With the fitting parameters we can calculate the rapidity density (dN/dy) by extrapolating to the whole p_T region. Figure 8 shows the rapidity distributions of leading baryons at 19 GeV/c. The error bars shown in the rapidity density distributions include both statistical and systematic contributions.

Figure 9 shows the ratio of the proton rapidity distribution to that of the neutrons at 19 GeV/c. The ratios in the rapidity region $2.3\leqslant y\leqslant 3.3$ are approximately between 1.0 and 2.3 and increase with rapidity. A few comments related to the proton/neutron ratio are in order. First, the ratio quickly approaches one at $y=2.3$, indicating that the projectile proton has a large probability to become a neutron through the isospin exchange interaction. Second, the large isospin exchange interaction cross section may contribute to chemical equilibration in relativistic heavy ion collisions. But the proton/neutron ratio near unity alone may not be sufficient experimental evidence for a full chemical equilibrium. It is interesting to note that the ratios have no significant target dependence, which implies that in the measured kinematic region the relative fragmentation probability of the incident proton into protons and neutrons does not depend on the target mass.

Figure 10 shows relative yields of neutrons and protons for different targets as a function of rapidity normalized to

TABLE I. Inverse slope parameters in MeV in $p+$Be, $p+$Al, $p+$Cu and $p+$Pb collisions at 19 GeV/c.

Rapidity	2.3	2.5	2.7	2.9	3.1	3.3
Neutron, Be	123±4	118±6	124±4	116±3	104±3	79±2
Proton, Be	137±8	137±5	130±4	127±4	108±1	88±2
Neutron, Al	128±4	120±4	123±3	118±3	105±3	80±2
Proton, Al	135±8	136±5	134±5	126±5	110±2	89±2
Neutron, Cu	132±5	120±6	123±5	118±5	111±4	82±2
Proton, Cu	137±8	136±5	136±5	132±6	112±3	90±2
Neutron, Pb	126±3	118±6	124±5	119±6	112±5	82±1
Proton, Pb	129±8	136±4	133±5	134±5	114±3	92±2

TABLE II. Inverse slope parameters in MeV in $p+$Be and $p+$Pb collisions at 12 GeV/c.

Rapidity	2.3	2.5	2.7	2.9	3.1
Neutron, Be	129±28	114±25	108±18	87±17	50±10
Proton, Be	126±21	136±20	130±15	88±10	67±8
Neutron, Pb	111±21	111±23	101±19	76±14	56±7
Proton, Pb	132±20	119±17	108±11	88±9	50±6

the yields in $p+$Be. While $(dN/dy)_{pA}/(dN/dy)_{p\mathrm{Be}}$ changes for different targets, for a given target, the ratios for protons and neutrons are the same within our experimental uncertainties. This universal target scaling was also observed for other particle species in previous measurements; see Ref. [22].

In Fig. 11, the E941 leading proton and neutron yields for $p+$Be and $p+$Pb at 19 GeV/c are compared with RQMD version 2.3c (without the mean field). The RQMD calculation fails to reproduce either our neutron or proton data. In the large rapidity region RQMD overestimates our data by about 40%. The E941 data indicate a greater baryon stopping in $p+A$ collisions at AGS energies than predicted by RQMD.

The energy scaling of leading proton production in $p+p$ collisions was originally considered to be an indication of the existence of constituent partons in the colliding protons [23]. The fragmentation of these partons continues to be an interesting experimental topic. We investigated the energy scaling of leading baryon production in $p+A$ collisions at AGS energies by plotting our data at two beam momenta as a function of the positive light cone variable $x_+ \equiv (E+p_\parallel)_l/(E+p_\parallel)_b$, where $(E+p_\parallel)_l$ and $(E+p_\parallel)_b$ stand for the longitudinal light cone momentum of leading baryons and beam protons, respectively. x_+ is therefore the fraction of the beam longitudinal light cone momentum carried away by the leading baryons. We chose x_+ because it is a Lorentz invariant quantity, thus making meaningful comparison among data

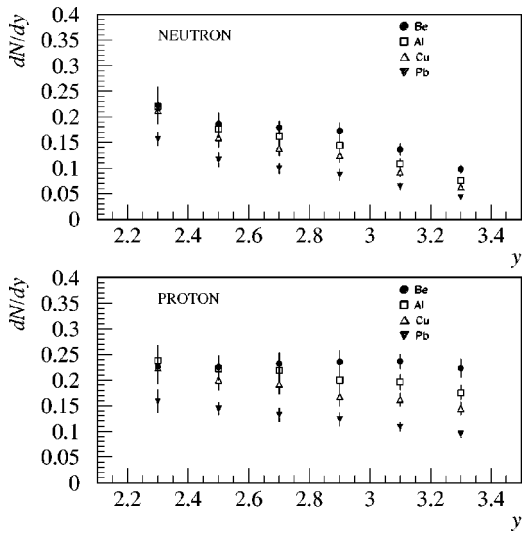

FIG. 8. Rapidity distributions of dN/dy for neutron and proton in $p+$Be, $p+$Al, $p+$Cu and $p+$Pb collisions at 19 GeV/c.

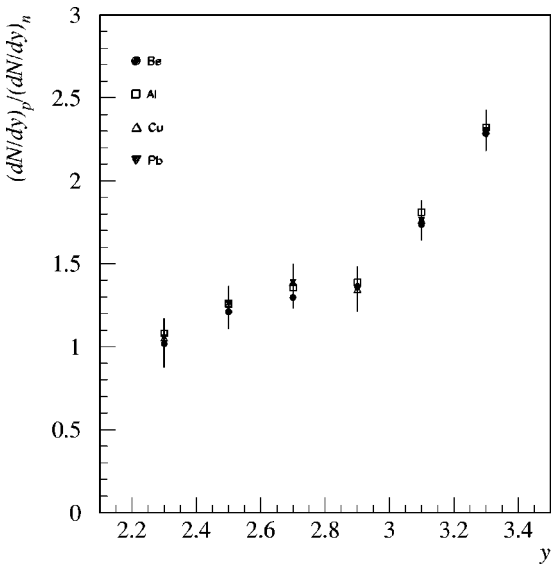

FIG. 9. p/n ratios as a function of rapidity in $p+$Be, $p+$Al, $p+$Cu, and $p+$Pb collisions at 19 GeV/c.

from different beam momenta possible. Figure 12 shows x_+ distributions of the leading proton and neutron at 12 GeV/c and 19 GeV/c. The results indicate energy scaling, i.e., the fragmentation function of the projectile into the leading baryon in $p+A$ collisions is independent of the projectile momentum in this energy region.

The proton/neutron ratio as a function of x_+ is also plotted in Fig. 13 for $p+$Be and $p+$Pb at 12 GeV/c and 19 GeV/c. The ratio scales very well for the two beam momenta. At high x_+ the ratio increases rapidly. This trend can be understood as the projectile proton has to replace a valence u quark with a d quark in order to become a leading neutron. Thus in an isospin exchange interaction, this replaced valence u quark may emerge as a leading meson carrying away a fraction of the initial momentum. Therefore,

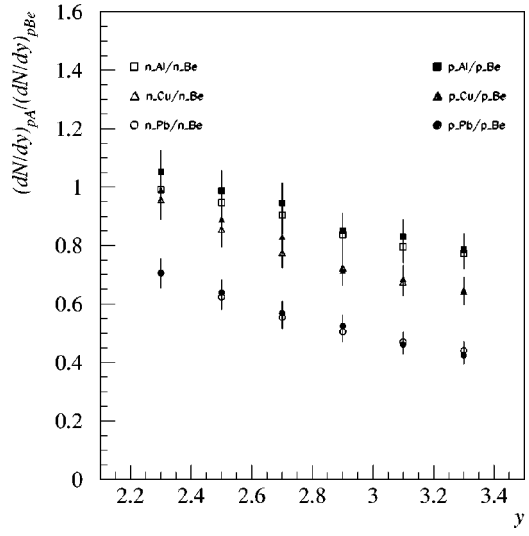

FIG. 10. Ratios of $(dN/dy)_{pA}/(dN/dy)_{p\mathrm{Be}}$ as a function of rapidity for proton (solid symbols) and neutron (open symbols) at 19 GeV/c.

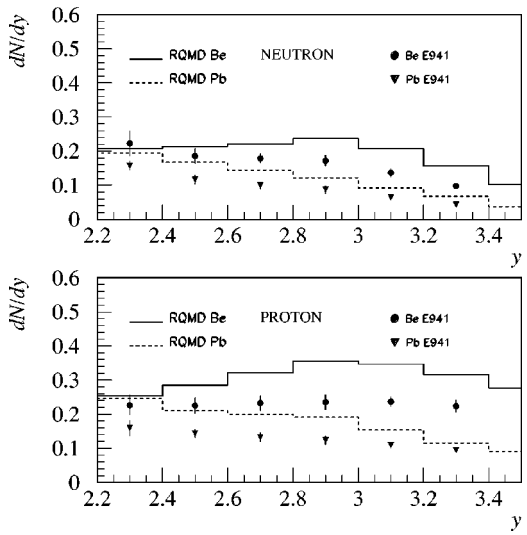

FIG. 11. Rapidity distributions of dN/dy for neutron and proton in $p+$Be and $p+$Pb collisions at 19 GeV/c compared with RQMD version 2.3c predictions.

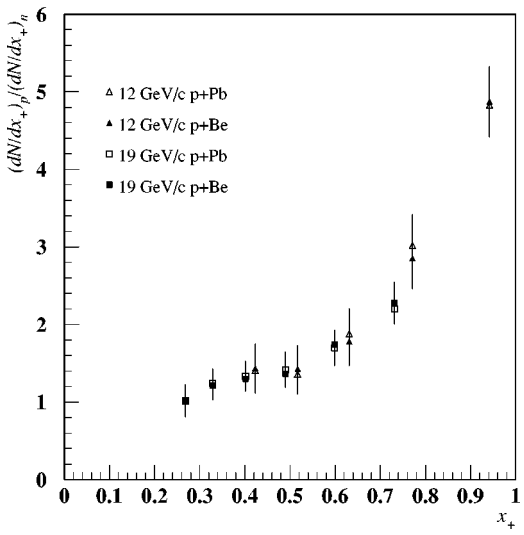

FIG. 13. p/n ratios as a function of x_+ in $p+$Be and $p+$Pb collisions at 12 GeV/c and 19 GeV/c.

leading neutron production near beam momentum is greatly suppressed. Within this quark fragmentation framework, the large p/n ratio at the high x_+ region also indicates that there is a considerable component of the leading proton spectra that does not result from the valence quark fragmentation process.

The target dependence of leading proton production in $p+A$ collisions at different energies has been previously studied [22]. It was found that the production cross section can be scaled $\propto A^{\alpha(x_F)}$, where $\alpha(x_F)=0.74-0.55x_F+0.26x_F^2$ and x_F is the Feynman variable ($x_F=2p_\parallel^*/\sqrt{s}$, where $p_\parallel^*$ and $\sqrt{s}$ are the longitudinal momentum in the center-of-mass (c.m.) frame of the nucleon-nucleon system and the c.m. energy, respectively). However, the energy scaling was not well established due to the large error bars of the data used in Ref. [22]. Note that the Feynman x_F has been used to describe data mostly for nucleon-nucleon collisions in the past, where the x_F is defined as the fraction of the beam momentum carried by the leading proton in the c.m. frame. For $p+A$ collisions the c.m. frame is not well defined; sometimes, the nucleon-nucleon c.m. frame is used for $p+A$ collisions. However, for the beam momentum larger than 100 GeV/c, there is little difference between x_+ and x_F in the region of x_+ above 0.2 or so.

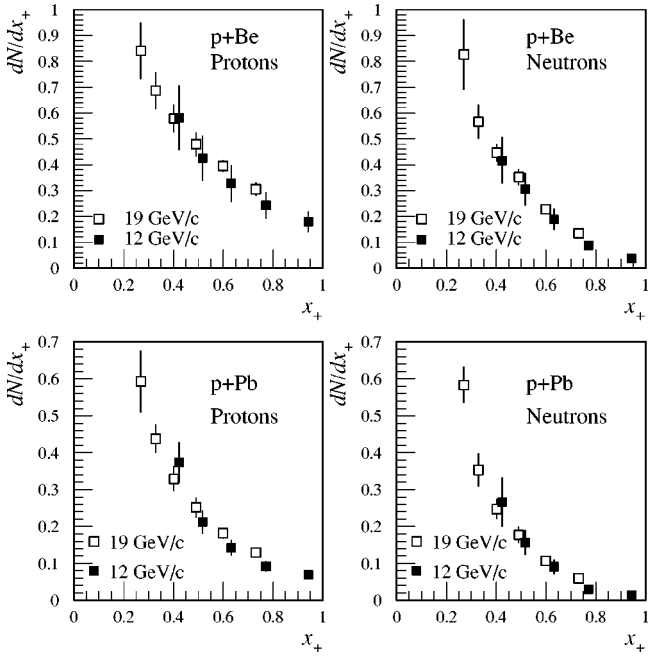

FIG. 12. dN/dx_+ distributions of the leading neutron (the right panels) and proton (the left panels) in $p+$Be and $p+$Pb collisions at 12 GeV/c and 19 GeV/c.

We also compare the target dependence of the E941 proton data with data from the E802 experiment [9] at 14.6 GeV/c, a CERN experiment [8] at 120 GeV/c, and a Fermilab experiment [22] at 100 GeV/c. The data from these four experiments are plotted versus x_+. In order to transform the rapidity variable (used by E802 and E941) and Feynman x_F (used by the CERN experiment) into x_+ we have assumed that the mean transverse momentum of leading protons is 0.4 GeV/c at AGS energies and 0.5 GeV/c at 120 GeV/c. In practice, the resulting x_+ distributions are not sensitive to reasonable variations in the $\langle p_T\rangle$ for the x_+ region reported here.

Figure 14 shows $(dN/dx_+)_{pA_1}/(dN/dx_+)_{pA_2}$ as a function of x_+ from the E941 data in comparison with these from the E802 data at 14.6 GeV/c, the CERN data at 120 GeV/c and the Fermilab data at 100 GeV/c. For heavy targets, the E802 experiment used gold and the CERN experiment used uranium. Therefore, the E941 Pb target data are compared with the E802 $p+$Au data and the CERN $p+$U data. In addition, the Fermilab data are normalized to the C target data, while the others are normalized to the Be target data. Finally, the Fermilab data are measured at $p_T=0.3$ GeV/c while the other experimental data are integrated over all p_T,

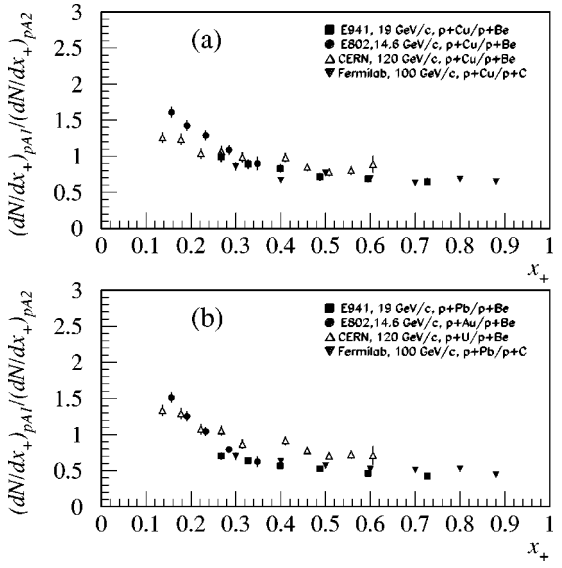

FIG. 14. The target dependence of the proton yields, $(dN/dx_+)_{pA_1}/(dN/dx_+)_{pA_2}$, as a function of the positive light cone variable x_+ for light targets (a) and heavy targets (b) in four experiments, E802 at 14.6 GeV/c, E941 at 19 GeV/c, CERN at 120 GeV/c and Fermilab at 100 GeV/c.

but it is found that the target dependence of the leading proton production in $p+A$ interactions has little p_T dependence [22].

We conclude from Fig. 14(a) that the target dependence of proton production in $p+\mathrm{Cu}$ collisions has an energy scaling from AGS energies to the CERN energy for $x_+ > 0.25$. Figure 14(b) indicates that such energy scaling may be approximately true for heavy targets.

However, a few comments are in order. In terms of the light cone momentum fraction variable, the x_+ range $[<(m_T/m_0)\exp(-y_b/2)]$, where the nucleons from target and projectile both contribute significantly, depends on the beam momentum. For example, at AGS momenta, target nucleons in $p+A$ collisions contribute significantly at x_+ around 0.2 or smaller, while at 120 GeV/c incident momentum, target nucleons only contribute to the x_+ below 0.1. Thus, both the E941 data and the CERN data are the measurement of the x_+ distribution from the projectile fragmentation in $p+A$ collisions. The E802 data, however, have significant contributions from the target. Therefore, the target contribution in the E802 data may explain the difference between the CERN and the E802 data at $x_+ < 0.25$ in Fig. 14(a), while at x_+ around 0.3, where the E941 and E802 data overlap, the E802 data and the E941 data agree very well. In addition, a systematic discrepancy between the CERN data and the Fermilab data is also noticed for heavy targets. Even if x_F is used, as in Ref. [22], instead of x_+ for the comparison, the discrepancy persists. Therefore, more data are needed to precisely test the energy scaling for heavy targets in the energy region between the AGS and the SPS.

In addition to fragmentation dynamics for the projectile breakup, it is believed that there could be novel mechanisms for baryon number transport in nuclear collisions in which the baryon number associated with the projectile or target is stopped at midrapidity via a gluon junction interaction [24–26]. The flavor changing reactions $p+A \rightarrow n(\Lambda)+X$ are believed to be sensitive to these new mechanisms of baryon stopping. A definitive measurement of the gluon junction interaction may come from exclusive measurements of high energy $p+A$ collisions where leading mesons and the stopped baryons are all identified [27]. It is unlikely that the gluon junction interaction could be studied unambiguously with the existing $p+A$ data. Our systematic measurements of the leading protons and neutrons will better constrain the traditional fragmentation functions.

IV. SUMMARY

We have presented a systematic measurement of leading protons and neutrons in $p+A$ collisions at 12 GeV/c and 19 GeV/c. The leading protons and neutrons from the projectile fragmentations show similar global features in rapidity and transverse mass spectra. The ratio of protons to neutrons, $(dN/dx_+)_p/(dN/dx_+)_n$, is about 5.0 near the beam rapidity and quickly approaches 1.0 around midrapidity. There is no strong target dependence in the p/n ratio as a function of rapidity. The x_+ distribution of leading baryons at AGS energies seems to exhibit beam energy scaling. The target dependence of the leading proton distribution as a function of x_+ shows an approximate energy scaling from AGS momenta to 120 GeV/c.

ACKNOWLEDGMENTS

We gratefully acknowledge the excellent support of the AGS staff. This work was supported in part by grants from the U.S. Department of Energy's High Energy and Nuclear Physics Divisions and the U.S. National Science Foundation.

[1] W. Busza and A.S. Goldhaber, Phys. Lett. **139B**, 235 (1984).
[2] The E814 Collaboration, J. Barrette *et al.*, Phys. Rev. C **50**, 3047 (1994); the E877 Collaboration, J. Barrette *et al.*, *ibid.* **62**, 024901 (2000); the E802 Collaboration, L. Ahle *et al.*, *ibid.* **57**, R466 (1998); the E917 Collaboration, B.B. Back *et al.*, Phys. Rev. Lett. **86**, 1970 (2001); the E864 Collaboration, T.A. Armstrong *et al.*, Phys. Rev. C **61**, 064908 (2000).
[3] W. Busza and R.J. Ledoux, Annu. Rev. Nucl. Part. Sci. **38**, 119 (1989).
[4] F. Videbaek and O. Hansen, Phys. Rev. C **52**, 2684 (1995).
[5] D. Dekkers *et al.*, Phys. Rev. **137**, B962 (1965).
[6] T. Eichten *et al.*, Nucl. Phys. **B44**, 333 (1972).
[7] W.S. Toothacker *et al.*, Phys. Lett. B **197**, 295 (1987).
[8] R. Bailey *et al.*, Z. Phys. C **29**, 1 (1985).

[9] E802 Collaboration, T. Abbott *et al.*, Phys. Rev. D **45**, 3906 (1992).
[10] E910 Collaboration, I. Chemakin *et al.*, nucl-ex/9902009; E910 Collaboration, B.A. Cole *et al.*, Nucl. Phys. **A661**, 366 (1999).
[11] H. Sorge, Phys. Rev. C **52**, 3291 (1995).
[12] K. Werner, Phys. Rep. **232**, 87 (1993).
[13] S. Date, M. Gyulassy, and H. Sumiyoshi, Phys. Rev. D **32**, 619 (1985).
[14] T.K. Choi, M. Maruyama, and F. Takagi, Phys. Rev. C **55**, 848 (1997).
[15] M. Gyulassy, Nucl. Phys. **A590**, 431c (1995).
[16] T.A. Armstrong *et al.*, Nucl. Instrum. Methods Phys. Res. A **437**, 222 (1999).
[17] T.A. Armstrong, R.A. Lewis, J. Passaneau, G.A. Smith, J.D. Reid, J. Stell, and W.S. Toothacker, Nucl. Instrum. Methods Phys. Res. A **425**, 210 (1999).
[18] T.A. Armstrong *et al.*, Nucl. Instrum. Methods Phys. Res. A **406**, 227 (1998).
[19] P. Haridas, I.A. Pless, G. Van Buren, J. Tomasi, M.S.Z. Rabin, K. Barish, and R.D. Majka, Nucl. Instrum. Methods Phys. Res. A **385**, 413 (1997).
[20] J.C. Hill *et al.*, Nucl. Instrum. Methods Phys. Res. A **421**, 431 (1999).
[21] E864 Collaboration, T.A. Armstrong *et al.*, Phys. Rev. C **60**, 064903 (1999).
[22] D.S. Barton *et al.*, Phys. Rev. D **27**, 2580 (1983).
[23] F.E. Taylor *et al.*, Phys. Rev. D **14**, 1217 (1976).
[24] D. Kharzeev, Phys. Lett. B **378**, 238 (1996).
[25] A. Capella and B. Kopeliovich, Phys. Lett. B **381**, 325 (1996).
[26] J. Ranft, hep-ph/0002137.
[27] H. Z. Huang, *Proceedings of the Relativistic Heavy Ion Symposium, APS Centennial Meeting '99, Atlanta, 1999* (World Scientific, Singapore, 1999), p. 3.